PAMM

WILEY-VCH

SPECIAL ISSUE 94th Annual Meeting of the International Association of Applied Mathematics and Mechanics (GAMM)

PAMM Proceedings in Applied Mathematics and Mechanics

RESEARCH ARTICLE OPEN ACCESS

A Trust-Region Method for *p*-Harmonic Shape Optimization

Henrik Wyschka | Winnifried Wollner

Department of Mathematics, University of Hamburg, Hamburg, Germany

Correspondence: Henrik Wyschka (henrik.wyschka@uni-hamburg.de)

Received: 19 July 2024 | **Revised:** 16 December 2024 | **Accepted:** 8 January 2025

Funding: The authors acknowledge the support by the Deutsche Forschungsgemeinschaft (DFG) within the Research Training Group GRK 2583 "Modeling, Simulation and Optimization of Fluid Dynamic Applications".

ABSTRACT

The appropriate scaling of deformation fields has a significant impact on the performance of shape optimization algorithms. We introduce a pointwise gradient constraint to an efficient algorithm for p-Laplace problems, while the complexity of the algorithm remains polynomial. Using this algorithm, we compute descent directions for shape optimization using p-harmonic approach that fulfill a trust-region type constraint. Numerical experiments show the advantages of deformations computed with this approach when compared to deformations that are scaled after computation. This considers, in particular, the approximation of the limit setting and the preservation of mesh quality during an optimization with a fixed step size.

1 | Introduction

In shape optimization constrained to partial differential equations (PDEs), we consider in general problems of the type

$$\begin{aligned} \arg\min_{\Omega\in\mathcal{A}} \quad & J(\Omega, y) \\ \text{s.t.} \quad & \mathcal{E}(\Omega, y) = 0 \\ & \mathcal{G}(\Omega) \quad = 0 \end{aligned}$$

where $J(\Omega, y)$ denotes the shape or objective functional depending on a shape Ω and a state y. The functional is constrained by a partial differential equation $\mathcal{E}(\Omega, y)$, as well as further geometric requirements $\mathcal{G}(\Omega)$. This type of problem opens up to wide range of applications including industrial relevance, see e.g., [1–7]. An optimal shape is reached via a sequence of updates to an initial shape by perturbations of identity $\Omega^{k+1} = (\mathrm{id} + tv)\,\Omega^k$ [8, 9]. This procedure requires two main components: first, a descent vector field $v : \mathbb{R}^d \to \mathbb{R}^d$ in a suitable sense, and second, a step size $t \in \mathbb{R}$, which then implicitly define the set of admissible shapes $\mathcal{A}$. Challenges in this regard usually consider the choice of appropriate shape spaces [10], the mesh quality during the optimization [11], as well as the computational costs [12].

Recent developments show remarkable results using steepest descent in a $W^{1,\infty}$-topology [13] as well as relaxations using the so-called p-harmonic approach [14]. This considers, in particular, the representation of sharp corners as well as the overall mesh quality. In this approach, we obtain the deformation field as the solution of an auxiliary minimization problem for $2 \le p < \infty$ reading

$$\arg\min_{v\in W^{1,p}(\Omega,\mathbb{R}^d)} \frac{1}{p}\int_\Omega \|\nabla v\|_2^p \,\mathrm{d}x + J'(\Omega)\,v \tag{1}$$

where $J'(\Omega)$ denotes the shape derivative of the reduced shape functional, assuming the existence of a suitable control-to-state operator. However, solving this problem is computationally costly and faces numerical challenges for higher orders $p > 5$. Thus, current work is devoted to finding an efficient algorithm for this type of problems [15].

Furthermore, the obtained deformation fields need to be scaled before application to the current shape. Commonly this can be done via an Armijo line-search [16]. But depending on the problem, this can also be computationally expensive, since it requires the evaluation of the shape functional and thus the

solution to primal as well as adjoint PDE in each iteration. Therefore, we suggest using a trust-region approach [16, 17] to obtain properly scaled deformation fields from the auxiliary problem. Motivated by additional constraints proposed in the limit setting for $p = \infty$ [18] as well as the structure of the present algorithm, we incorporate a semi-norm-type bound to the p-Laplacian algorithm. This then corresponds to a problem with pointwise gradient constraints [19, 20].

Within this article, we introduce the changes required to the algorithm for the p-Laplacian in Section 2 and show numerical results with fixed gradient bounds in Section 3. Theoretical results for the algorithm as well as numerical results including updates of the step size will be provided in an upcoming paper.

2 | Algorithm

As the base for the integration of the trust-region constraint, we use the previously presented vector-valued extension of an efficient algorithm for the p-Laplace problem [15, 21]. For this algorithm, we assume that part of the domain boundary $\partial\Omega \setminus \Gamma$ is fixed with Dirichlet boundary conditions, commonly homogenous in shape optimization applications. Further, a part of the boundary Γ is free for deformation, and the shape derivative can be expressed as integrals over this part of the boundary and the domain. These assumptions create a reasonable setting to cover relevant applications. See [22] for an example using boundary formulation, including geometric constraints, as well as [23] for an extensive discussion on domain formulations. The auxiliary problem (1) then reads

$$\arg\min_{u \in \mathcal{U}^p} J_p(u) = \frac{1}{p} \int_\Omega \|\nabla(u+g)\|_2^p \, \mathrm{d}x - \int_\Gamma hu \, \mathrm{d}\bar{x} - \int_\Omega fu \, \mathrm{d}x, \tag{2}$$

where $\mathcal{U}^p := \{u \in \mathrm{W}^{1,p}(\Omega, \mathbb{R}^d) : u = 0 \text{ a.e. on } \partial\Omega \setminus \Gamma\}$ and non-homogenous Dirichlet boundary conditions could be included by an arbitrary prolongation g to the whole domain $v := u + g$. However, in the context of trust-region for shape optimization, we focus on homogenous Dirichlet conditions to fix parts of the boundary and thus only consider the prolongation $g \equiv 0$ here. We observe that the first term

$$\|v\|^p_{\mathrm{X}^p(\Omega,\mathbb{R}^d)} := \int_\Omega \|\nabla v\|_2^p \, \mathrm{d}x$$

describes an equivalent semi-norm on $\mathrm{W}^{1,p}(\Omega, \mathbb{R}^d)$ as well as an equivalent norm on $\mathrm{W}^{1,p}_0(\Omega, \mathbb{R}^d)$ and in particular on $\mathcal{U}^p$. Thus, this norm would be a suitable candidate for the trust-region constraint. However, we want to discuss the benefits of using a pointwise approach corresponding to $\|v\|_{\mathrm{X}^\infty(\Omega,\mathbb{R}^d)} := \operatorname{ess\,sup}_{x\in\Omega} \|\nabla v\|_2$ in the following.

The base algorithm relies on discretizing the problem (2) by linear finite elements and reformulating this as the minimization of a scalar product over a convex and bounded set. Then, one can use results from classical convex optimization [24] and apply an interior-point method to solve the problem. A crucial step in this reformulation is the addition of an additional upper bound to the search set based on an a-priori estimate. The estimate also holds in a vector-valued setting as

$$\|u_k\|^p_{\mathrm{X}^p(\Omega,\mathbb{R}^d)} \le C_0 + C_1 \|g\|^p_{\mathrm{X}^p(\Omega,\mathbb{R}^d)} + C_2(\Omega, p) \, \|f\|^{p^*}_{\mathrm{L}^{p^*}(\Omega,\mathbb{R}^d)} + C_3(\Omega, p) \, \|h\|^{p^*}_{\mathrm{L}^{p^*}(\Gamma,\mathbb{R}^d)} =: \tilde{R}.$$

However, the direct addition of a bound in terms of $\|u\|_{\mathrm{X}^p(\Omega,\mathbb{R}^d)}$ leads to a rank-1-dense block in the Hessian used by the interior-point method. Instead, the bound is implemented as

$$\omega_i \|\nabla u|_{K_i}\|_2^p \le \tilde{R} \tag{3}$$

in a pointwise fashion for each finite element K_i with weight ω_i, resulting in a diagonal block. See the original publication [21] for more information on the benefits of this reformulation, as well as techniques for solving the dense system. Consequently, we implement the discrete trust-region constraint in the same pointwise way as

$$\|\nabla u|_{K_i}\|_2 \le \Pi. \tag{4}$$

By construction, the algorithm gives access to an auxiliary variable $s_i \ge \|\nabla(u+g)|_{K_i}\|_2^p$. Thus, there are multiple ways to set up barrier terms corresponding to this constraint for the interior-point method. We could canonically add $s_i^{1/p} \le \Pi$, which can have numerical benefits depending on the values, but results in two terms in the Hessian of the barrier function. Therefore, we can transfer the power to $s_i \le \Pi^p$ instead, which only results in one simple contribution to the Hessian. The reformulated problem is then constructed by naturally incorporating this constraint into the search set in [15, Lem. 9.1].

Lemma 2.1. *The problem (2) of minimizing $J_p(u)$ over a suitable finite element space V_{h_Ω} with $1 \le p < \infty$ subject to the additional constraints (3) and (4) is equivalent to the problem*

$$\arg\min_{x \in \mathcal{Q}^p} \langle c, x \rangle \quad \text{with } c = \begin{bmatrix} -Mf - \bar{M}h \\ \frac{1}{p}\omega \end{bmatrix}$$

and the constrained search set given by

$$\mathcal{Q}^p = \left\{ (u,s) \in \mathbb{R}^n \times \mathbb{R}^m : s_i^{\frac{2}{p}} \ge \sum_{j=1}^d \sum_{r=1}^d [D^{(j,r)}u]_i^2 \wedge s_i \ge 0 \wedge \omega_i s_i \le R \wedge s_i \le \Pi^p \right\}.$$

Here, M and $\bar{M}$ correspond to the mass matrix on domain and boundary respectively and $D^{(j,r)}$ is the discrete derivative matrix for component u_r in direction x_j.

The additional constraint can be written in the form $\theta_i := \Pi^p - s_i \ge 0$ and thus an additional barrier term and its derivatives can be set up as

$$F(u,s) = -\sum_i \log(\theta_i) \quad \text{with} \quad F_s(u,s) = \theta^{-1} \quad \text{and} \quad F_{ss}(u,s) = \operatorname{diag}(\theta)^{-2}. \tag{5}$$

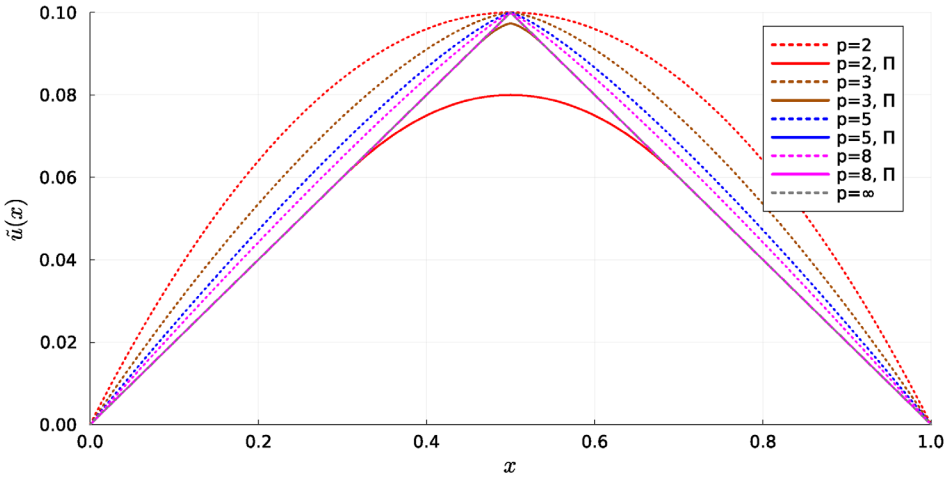

FIGURE 1 | Solution of one-dimensional p-Laplace problems with Dirichlet boundary condition $u(0) = u(1) = 0$ and source term $f \equiv 1$ for various parameters p. Each as unconstrained version normalized and scaled (dashed) or with gradient bound $|\nabla u| \leq 0.2 =: \Pi$.

We want to mention that by this construction we get two barrier terms corresponding to upper bounds on s_i. Thus, for practical computation, it could be beneficial to rephrase the a-priori bound to the slightly weaker form $s_i \leq \omega_{\min}^{-1} R$ and then only use one barrier term with the smaller bound and potential scaling instead.

Furthermore, we establish an extension of the convergence theorems [21, Theo. 1] and [15, Theo. 9.1] to the vector-valued setting, including pointwise gradient bounds, with the proof to be presented in a forthcoming article.

Theorem 2.2. *Let $2 \leq p < \infty$. Assume that $\Omega \subset \mathbb{R}^d$ is a Lipschitz polytope of width L with suitable triangulation T_{h_Ω}. Further, assume $f \in L^{p^*}(\Omega, \mathbb{R}^d)$ and $h \in L^{p^*}(\Gamma, \mathbb{R}^d)$. The algorithm described in [15], including the additional barrier terms (5), converges to the solution of the problem (2) subject to $\|u\|_{X^\infty(\Omega,\mathbb{R}^d)} \leq \Pi$ in at most $\mathcal{O}(\sqrt{n}\log(n))$ iterations.*

3 | Numerical Results

In this section, we want to illustrate some properties of solutions to the p-Laplace problem including a gradient constraint. In particular, we compare these solutions to solutions that are scaled accordingly after the computation. Based on a simple optimization with a fixed step size, we motivate the usage of a trust-region type method in p-harmonic shape optimization instead of scaling the deformation field by, e.g., line search.

As the first test case, we consider the 1-dimensional Laplacian on the unit interval (0,1) with homogeneous Dirichlet boundary conditions $v(0) = v(1) = 0$ and constant source term $\Delta_p v = \nabla \cdot (\|\nabla v\|_2^{p-2} \nabla v) = 1$. For this simple problem, the analytical solution in the limit $p = \infty$ is known as $v = u = \mathrm{dist}(x, \partial\Omega)$ and the solutions for finite p form a converging sequence to this limit [18]. A visualization of this setting can be found in [15, Fig. 9.4]. Here, we want to focus on the impact of the gradient constraint to the solution. Figure 1 shows solutions computed including the gradient bound $|\nabla u| \leq 0.2$ in comparison to solutions of the regular problem scaled to the same magnitude by $0.2 \frac{u}{\|u\|_\infty} \|\mathrm{dist}(x, \partial\Omega)\|_\infty$. We first observe, that the two solutions corresponding to the same p are not identical, but rather the gradient bound being the dominant factor for the slope of the solution. In particular, solutions computed including the constraint match the solution of the limit setting near the boundaries. Further, the differences in the solutions for increasing order p are reduced when the gradient constraint is included. With the deviations concentrated around the tip, there is no visible difference between $p = 5$ and $p = 8$.

In the second test case, we compute one single two-dimensional deformation field. For this, we consider the unit square with left and upper boundary free for deformation, as sketched in Figure 2a. On those boundaries, the Neumann boundary condition $h(x) = [\sin(2\pi x_1) - \sin(2\pi x_2)]\,\eta$ is prescribed, which corresponds to a force applied in normal direction. Figure 3 illustrates the magnitudes of the solutions for the regular p-Laplacian with increasing parameter p, computed on a uniform triangular grid with 10^4 nodes. We observe significant differences between the different solutions. The linear Laplacian $p = 2$ has an overall smaller magnitude and clearly shows contributions from the negative parts of the boundary condition. As expected, when increasing p, the contributions of the negative part reduce, and the solution on the boundary adjusts to a linear function. In the interior domain, consequently, the overall magnitude of the solution increases, while the level sets progress toward a sequence of nested squares.

As comparison, Figure 4 shows the magnitudes of solutions obtained with the p-Laplacian including the gradient constraint. The overall behavior of the sequence when increasing p has changed, and all solutions seem relatively similar. This indicates the dominance of the gradient constraint. In particular, the solution $p = 2$ differs completely. First note, that due to the constraint, this does not reduce to a linear problem anymore. Then, we observe that the solution on the free boundaries is similar to Figure 3d, the regular solution for $p = 8$. However, the interior domain is not developed as far. For that, we need to require $p = 3$ or $p = 5$. In particular, $p = 5$ seems sufficient and there is only a minimal difference to $p = 8$. For the application in p-harmonic shape optimization, these are interesting properties. Since the Neumann condition is applied on the design boundary,

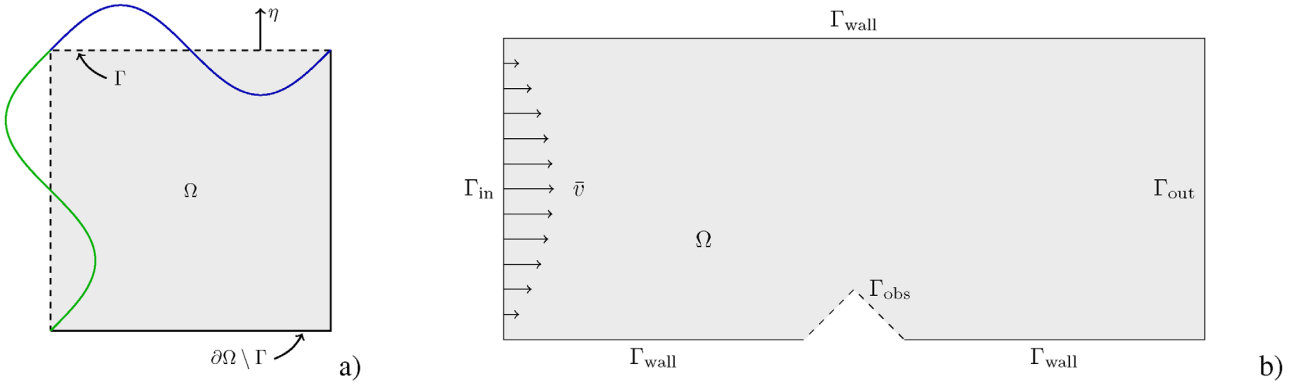

FIGURE 2 | Sketches of the domains for the two-dimensional test cases. Dashed boundaries indicate design areas. (a) describes a square domain with two free boundaries and the Neumann boundary conditions applied to them. (b) describes a flow channel with parabolic inflow and an obstacle on the bottom boundary.

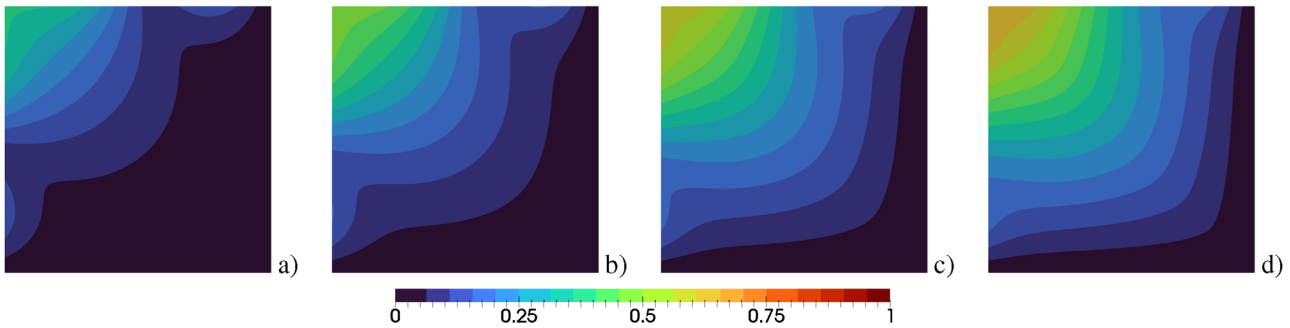

FIGURE 3 | Magnitude of the deformation fields obtained in the square test case for increasing parameters p, where (a) $p = 2$, (b) $p = 3$, (c) $p = 5$, and (d) $p = 8$.

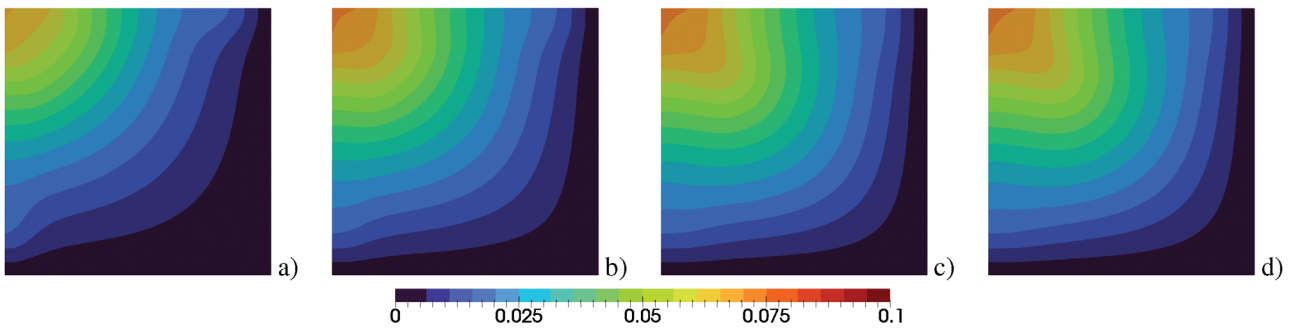

FIGURE 4 | Magnitude of the deformation fields obtained in the square test case with gradient bound $\|u\|_{X^\infty(\Omega,\mathbb{R}^d)} \leq 0.1$ for increasing parameters p, where (a) $p = 2$, (b) $p = 3$, (c) $p = 5$, and (d) $p = 8$.

we would automatically obtain shapes with better representation of sharp edges that are normally only archived for higher-order p.

Third, we consider an optimization related test case. We aim to minimize the energy dissipation of Stokes flow [25]

$$\arg\min_{\Omega\in\mathcal{A}} \int_\Omega \sum_{i,j=1}^{d} \left(\frac{\partial v_i}{\partial x_j}\right)^2 \mathrm{d}x \quad \text{s.t.} \quad \left.\begin{aligned} \Delta v + \nabla p &= 0 \quad \text{in } \Omega \\ \nabla \cdot v &= 0 \quad \text{in } \Omega \\ v &= \bar{v} \quad \text{on } \Gamma_{\text{in}} \\ v &= 0 \quad \text{on } \Gamma_{\text{wall}} \cup \Gamma_{\text{obs}} \end{aligned}\right\}. \tag{6}$$

in a channel with a bump on the bottom, as sketched in Figure 2b. The bump itself is the part of the boundary that is free for deformation, and thus we expect to remove the bump. We do not enforce geometric constraints, so the optimization problem is in general not well-posed for Stokes flow. However, it showcases some interesting properties of the deformations, since the gap in the channel boundary is smaller than the length of the design boundary. Thus, elements have to contract and then expand again without creating overlaps. The domain is discretized with 350 nodes and 629 elements, where the tip of the bump is slightly rounded for computational reasons. The optimization routine stops if two elements overlap or the update in the objective functional is smaller than 10^{-5}. The accuracy of the p-Laplace

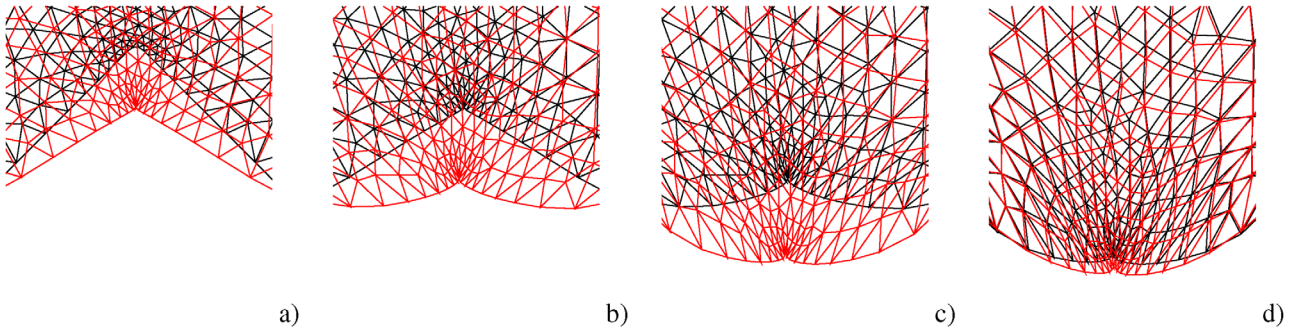

FIGURE 5 | Final deformation of the mesh at the tip of the design domain in the channel flow test case for increasing parameters p, where (a) $p = 2$, (b) $p = 3$, (c) $p = 5$, and (d) $p = 8$.

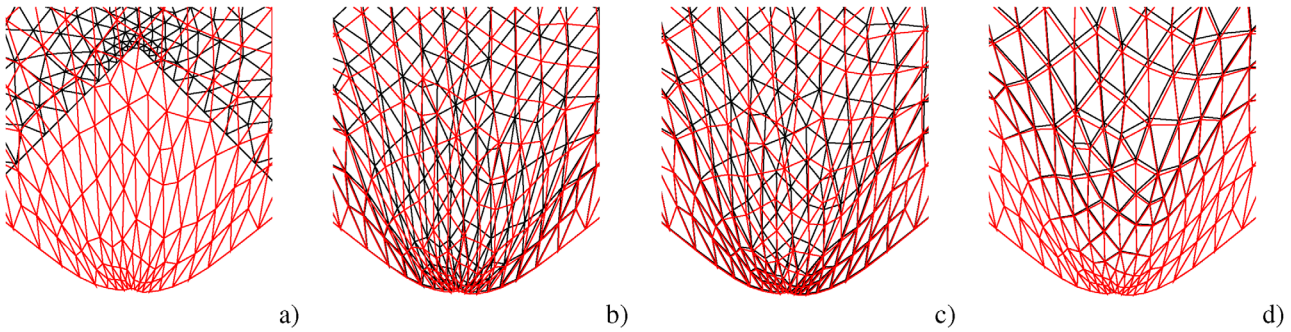

FIGURE 6 | Final deformation of the mesh at the tip of the design domain in the channel flow test case using a gradient bound for increasing parameters p, where (a) $p = 2$, (b) $p = 3$, (c) $p = 5$, and (d) $p = 8$.

extension solver is 10^{-9} and a step size of $t = 10^{-2}$ is used either for scaling or as the gradient bound.

Figure 5 shows the mesh around the tip of the kink at the end of the optimization. In the background, you see the obtained mesh for the previous p or the initial mesh if $p = 2$ for comparison. For $p = 2$ the optimization routine stopped because elements overlap, not yielding a reasonable solution. A similar behavior occurs for $p = 3$, although the overlap happens later in this setting. For $p = 5$ the optimization stops based on the convergence criteria and yields a reasonable solution. However, there is still a significant artifact around the elements that formed the tip in the initial shape. In the last setting for $p = 8$, we find a similar final shape, but there are some improvements. The overall volume is slightly increased, reducing the objective functional value, and the artifact becomes smaller.

Figure 6 shows the same optimizations as Figure 5, but computed with the p-Laplace algorithm, including the gradient constraint. First, we observe that all routines stop based on the convergence criterion, and the final shapes look similar. In particular, the shape for $p = 2$ is comparable to the non-constraint solution for $p = 8$ with the overall volume being slightly larger and the artifact further reduced. When increasing from $p = 2$ to $p = 3$ and further to $p = 5$, we observe again slight improvements around the artifacts. However, the main difference is in the interior domain, where the size of the elements becomes more evenly distributed, and the overall mesh quality is improved. In the last step, from $p = 5$ to $p = 8$, the overall changes become minimal and thus indicating no requirement for further increase.

4 | Conclusion

We added a gradient constraint to the extension problem for p-harmonic shape optimization and showed that a deformation field can still be computed efficiently. Further, we observed that the behavior of the resulting deformation fields is dominated by the gradient constraint, and they are comparable to those that are only archived for larger p in the non-constrained setting. Thus, indicating the benefits of using a trust-region-based approach in p-harmonic shape optimization. In experiments with fixed step size, we then showed that such an approach yields improvements with respect to the archived boundary design and the overall mesh quality. The detailed proof of the theorem and numerical results for a trust-region-based shape optimization including updates of the step size, i.e., the gradient constraint, will be provided in a forthcoming article.

Acknowledgments

The authors acknowledge the support by the Deutsche Forschungsgemeinschaft (DFG) within the Research Training Group GRK 2583 "Modeling, Simulation and Optimization of Fluid Dynamic Applications".

Open access funding enabled and organized by Projekt DEAL.

References

1. E. Wadbro, R. Udawalpola, and M. Berggren, "Shape and Topology Optimization of an Acoustic Horn–Lens Combination," *Journal of Computational and Applied Mathematics* 234, no. 6 (2010): 1781–1787.

2. S. Schmidt, C. Ilic, V. Schulz, and N. R. Gauger, "Three-Dimensional Large-Scale Aerodynamic Shape Optimization Based on Shape Calculus," *AIAA Journal* 51, no. 11 (2013): 2615–2627.

3. P. Gangl, U. Langer, A. Laurain, H. Meftahi, and K. Sturm, "Shape Optimization of an Electric Motor Subject to Nonlinear Magnetostatics," *SIAM Journal on Scientific Computing* 37, no. 6 (2015): B1002–B1025.

4. N. Kühl, T. T. Nguyen, M. Palm, D. Jürgens, and T. Rung, "Adjoint Node-Based Shape Optimization of Free-Floating Vessels," *Structural and Multidisciplinary Optimization* 65, no. 9 (2022): 247.

5. L. Schlegel and V. Schulz, "Shape Optimization for the Mitigation of Coastal Erosion via Porous Shallow Water Equations," *International Journal for Numerical Methods in Engineering* 123, no. 22 (2022): 5416–5441.

6. L. Radtke, G. Bletsos, N. Kühl, et al., "Parameter-Free Shape Optimization: Various Shape Updates for Engineering Applications," *Aerospace* 10, no. 9 (2023): 751.

7. S. Blauth, M. Baldan, S. Osterroth, et al., "Multi-Criteria Shape Optimization of Flow Fields for Electrochemical Cells," *Chemie Ingenieur Technik* 96, no. 5 (2024): 616–626.

8. J. Sokolowski and J.-P. Zolesio, *Introduction to Shape Optimization*, Springer Series in Computational Mathematics (Berlin, Heidelberg: Springer, 1992).

9. M. C. Delfour and J.-P. Zolesio, *Shapes and Geometries: Metrics, Analysis, Differential Calculus, and Optimization*, Advances in Design and Control, Vol. 22, 2nd ed. (Philadelphia: SIAM, 2011).

10. K. Welker, "Suitable Spaces for Shape Optimization," *Applied Mathematics and Optimization* 84, no. 1 (2021): 869–902.

11. S. Onyshkevych and M. Siebenborn, "Mesh Quality Preserving Shape Optimization Using Nonlinear Extension Operators," *Journal of Optimization Theory and Applications* 189, no. 1 (2021): 291–316.

12. P. M. Müller, J. Pinzón, T. Rung, and M. Siebenborn, "A Scalable Algorithm for Shape Optimization with Geometric Constraints in Banach Spaces," *SIAM Journal on Scientific Computing* 45, no. 2 (2023): B231–B251.

13. K. Deckelnick, P. J. Herbert, and M. Hinze, "A novel $W^{1,\infty}$ Approach to Shape Optimisation With Lipschitz Domains," *ESAIM: Control, Optimisation and Calculus of Variations* 28 (2022): 2.

14. P. M. Müller, N. Kühl, M. Siebenborn, K. Deckelnick, M. Hinze, and T. Rung, "A Novel *p*-Harmonic Descent Approach Applied to Fluid Dynamic Shape Optimization," *Structural and Multidisciplinary Optimization* 64 (2021): 3489–3503.

15. H. Wyschka and M. Siebenborn, "Towards Computing High-Order p-Harmonic Descent Directions and Their Limits in Shape Optimization," in *Modeling, Simulation and Optimization of Fluid Dynamic Applications*, eds. A. Iske and T. Rung (Cham: Springer, 2023), 147–163.

16. J. Nocedal and S. J. Wright, *Numerical Optimization*, Springer Series in Operations Research and Financial Engineering 2 ed. (New York: Springer, 2006).

17. A. R. Conn, N. I. M. Gould, and P. L. Toint, *Trust Region Methods*, MPS/SIAM Series on Optimization, Vol. 1 (Philadelphia: Society for Industrial and Applied Mathematics, 2000).

18. H. Ishii and P. Loreti, "Limits of Solutions of *p*-Laplace Equations as *p* Goes to Infinity and Related Variational Problems," *SIAM Journal on Mathematical Analysis* 37, no. 2 (2005): 411–437.

19. C. Ortner and W. Wollner, "A Priori Error Estimates for Optimal Control Problems With Pointwise Constraints on the Gradient of the State," *Numerische Mathematik* 118, no. 3 (2011): 587–600.

20. A. Günther and M. Hinze, "Elliptic Control Problems With Gradient Constraints—Variational Discrete Versus Piecewise Constant Controls," *Computational Optimization and Applications* 49, no. 3 (2011): 549–566.

21. S. Loisel, "Efficient Algorithms for Solving the *p*-Laplacian in Polynomial Time," *Numerische Mathematik* 146, no. 2 (2020): 369–400.

22. V. Schulz and M. Siebenborn, "Computational Comparison of Surface Metrics for PDE Constrained Shape Optimization," *Computational Methods in Applied Mathematics* 16, no. 3 (2016): 485–496.

23. R. Hiptmair, A. Paganini, and S. Sargheini, "Comparison of Approximate Shape Gradients," *BIT Numerical Mathematics* 55 (2015): 459–485.

24. Y. Nesterov and A. S. Nemirovskii, *Interior-Point Polynomial Algorithms in Convex Programming*, SIAM Studies in Applied Mathematics, Vol. 13, 3rd ed. (Philadelphia: SIAM, 2001).

25. B. Mohammadi and O. Pironneau, *Applied Shape Optimization for Fluids*, Numerical Mathematics and Scientific Computation, 1st ed. (Oxford: Oxford University Press, 2001).